Cylindrical glass nanocapillaries patterned via coarse lithography (>1 μm) for biomicrofluidic applications

Yifan Liu and Levent Yobas[a)]
Department of Electronic and Computer Engineering, Hong Kong University of Science and Technology, Clear Water Bay, Kowloon, Hong Kong

(Received 18 September 2012; accepted 27 November 2012; published online 13 December 2012)

We demonstrate a new method of fabricating in-plane cylindrical glass nanocapillaries (<100 nm) that does not require advanced patterning techniques but the standard coarse photolithography (>1 μm). These nanocapillaries are self-enclosed optically transparent and highly regular over large areas. Our method involves structuring μm-scale rectangular trenches in silicon, sealing the trenches into enclosed triangular channels by depositing phosphosilicate glass, and then transforming the channels into cylindrical capillaries through shape transformation by the reflow of annealed glass layer. Extended anneal has the structures shrunk into nanocapillaries preserving their cylindrical shape. Nanocapillaries ~50 nm in diameter and effective stretching of digested λ-phage DNA in them are demonstrated. © *2012 American Institute of Physics*. [http://dx.doi.org/10.1063/1.4771691]

I. INTRODUCTION

Nanofluidics, emerged recently in the footsteps of microfluidics, has been drawing great attention as a promising tool to detect and manipulate biomolecules.[1,2] New effects have been revealed in nanoscale fluidic channels such as physical confinement of macromolecules (e.g., nucleic acids)[3,4] and unique ionic transport mechanisms,[5–7] which fuel numerous innovative studies. In particular, the static and dynamic properties of single DNA molecule confined in nanochannels ranging from tens to hundreds of nanometers have been well characterized,[8] and applications including DNA stretching[9,10] and DNA entropic trapping[11] have been reported. Moreover, the nanofluidic ionic current diodes[12–17] and ionic field effect transistors[18,19] have been developed as active nano-electronic-fluidic devices that could possibly lead the way to a diverse set of applications ranging from biosensing[20,21] to transport of molecules.[22]

To pattern nanochannels, silica-based (e.g., silicon, glass, quartz) substrates are most commonly preferred due to their robustness and compatibility with microelectronics fabrication technologies. Till now, a broad range of methods has been developed to create nanochannels on such platforms. Among those, high-resolution lithography, mainly electron beam lithography (EBL)[23,24] and nanoimprint lithography (NIL)[25] are often employed to pattern nanotrench structures that can be subsequently turned into enclosed nanochannels by using approaches such as wafer bonding,[26] polymer reflow,[27] laser pulse melting,[28] and atomic layer deposition.[29] EBL, although it allows a precise and uniform patterning of nanostructures, is relatively expensive and suffers from limited throughput, especially when it comes to writing dense array of patterns over a large area. NIL has been successfully demonstrated for wafer-scale fabrication but thus far faced issues with defects produced by the mold deformation, uneven coating during the process, and cumbersome preparation of the imprint template.[30] Thus, it is of utmost priority that new fabrication techniques are introduced so as to form nanochannels without resorting to advanced lithography methods.

Previously, glass thermal reflow has been introduced as a route to fabricating micro/nanochannels via transforming triangular voids trapped within a glass layer into round in-plane

[a)]Author to whom correspondence should be addressed. Electronic mail: eelyobas@ust.hk. Tel.: (+852) 2358–7068.

 © 2012 American Institute of Physics

capillaries.[31] Such voids, which are formed by non-conformal deposition of glass fillings on microstructured silicon, are rounded during thermal anneal as a result of glass reflow that minimizes the surface energy. Based on the principle, we have demonstrated cylindrical glass microcapillaries[32] and their on-chip integration to perform cellular electrophysiology analysis[33] and highly effective capillary electrophoresis.[34] Sub-100 nm cylindrical nanochannels have also been fabricated through this approach, albeit applying advanced lithography to register silicon trenches 300 nm wide.[31]

Here, we extend the glass thermal reflow process to the fabrication of cylindrical nanocapillaries on substrates patterned by conventional coarse (resolution $> 1\,\mu$m) photolithography. Our work draws its principle from an age-old method of forming isolated nanochannels/nanopores—the glass nanopipette.[35] Glass nanopipette fabrication begins with a thin-wall capillary having a typical diameter well above 100 μm. The capillary is heated around its midpoint to briefly exceed its glass transition temperature while both ends are being pulled to stretch and thin the capillary until it splits into two pieces each having a tip opening diameter below 100 nm. Transferring this principle on a planar platform whereby the required external forces that drive the shape transformation are delivered from the surface energy of as-deposited glass, defined by the topography of the underlying substrate, we first mould self-sealed channel precursors in a glass layer on microstructured silicon substrates and demonstrate their controlled shrinking into cylindrical nanocapillaries.

The principle of our approach is schematically described in Fig. 1. As depicted in Fig. 1(a), buried triangular voids are trapped within silicon trenches by non-conformal deposition of glass on microstructured silicon substrate. During thermal reflow, the glass layer is softened and the voids begin to evolve under the surface tension of the viscous glass. Sharp corners with a high surface curvature get preferentially smoothened, returning channel cross-sections initially elliptic as in Fig. 1(b) and then fully round having a uniform surface curvature and minimized surface energy as in Fig. 1(c). Above steps roughly illustrate the mechanism of cylindrical channel formation realized in previous studies.[31,32] However, it should be noted that gas pressure inside the rounded voids is insufficient to balance the Laplace pressure induced by the surface tension at the gas-glass interface such that the surrounding viscous glass can continue to squeeze in, further shrinking the voids, eventually filling the trenches completely. This self-shrinking evolution of buried channels, if controlled precisely, can be terminated at an opportune moment that offers cylindrical capillaries with a desired diameter at a sub-lithographic dimension, a fraction of the initially patterned trench width [Fig. 1(d)]. Utilizing this principle, we have successfully fabricated cylindrical nanocapillaries and managed to control the capillary

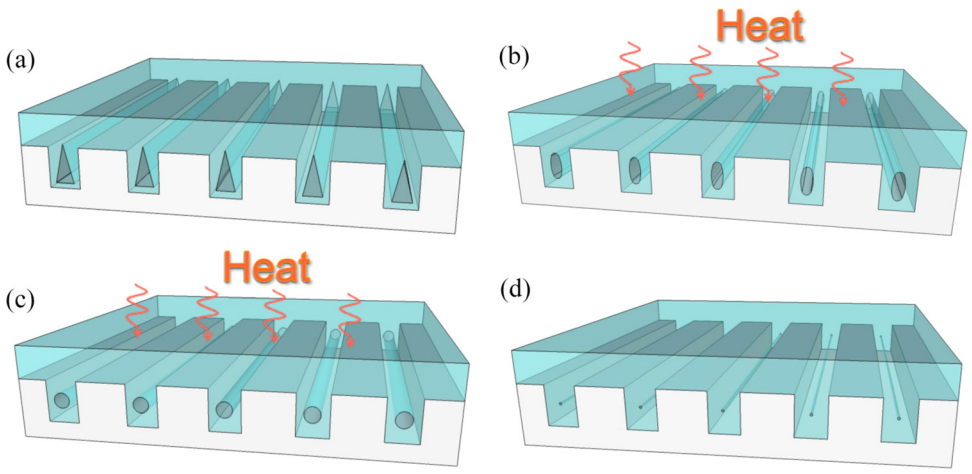

FIG. 1. Conceptual illustration of the process of forming self-enclosed cylindrical nanocapillaries: (a) triangular voids being trapped within rectangular trenches through non-conformal deposition of the glass filling; (b) and (c) the same voids after being transformed into first elliptical and then round capillaries via annealed glass reflow process; (d) continued reflow with the precise control of the reflow time shrinks the round capillaries into nanocapillaries.

diameter from sub-micron to tens of nanometers. In addition, we have also demonstrated these transparent nanocapillaries for stretching DNA. This approach offers great potential to integrate new nanofluidic devices for various biomicrofluidic applications.

II. THEORY AND MODELING

Glass is an amorphous material that mechanically behaves like a solid in room temperature yet lacks the periodicity of a crystal. It transits from a solid-like brittle state to a molten rubber-like state undergoing a thermal process. Unlike the sudden melt of a crystal observed at a consistent temperature, the transition of glass extends over a broad range of temperature with a gradual decrease in its shear viscosity. For a certain type of glass, the transition temperature (T_g) is defined as the point at which its viscosity drops to 10^{12} Pa s and gets extremely sensitive to temperature variations. Thermal reflow is typically conducted at $T > T_g$ whereby glass is molten into a viscous liquid. During this process, forces acting either on the bulk (e.g., gravity) or at the interface (e.g., surface tension) drive the glass reflow towards the profile of minimum energy. This viscous flow of glass can be described by the Navier-Stokes (N-S) equations.

Here, the glass thermal reflow that leads to the formation of nanocapillaries is modeled as an incompressible surface tension driven viscous flow in two dimensions (assuming infinitely long trenches). Due to the small geometry, high viscosity, and low velocity, the Reynolds number, which is the ratio of inertial forces to viscous forces, is typically much less than 1 ($Re \ll 1$), thereby, inertial parts in the N-S equations can be ignored reducing the model into a 2-D creeping flow governed by the Stokes equations

$$\rho \frac{\partial \mathbf{v}}{\partial t} + \nabla p = \mu \nabla^2 \mathbf{v}, \tag{1}$$

where p is the pressure on the fluid bulk, $\mathbf{v}$ is the velocity vector of fluid, and ρ and μ are the density and the shear viscosity of the fluid, respectively.

Given the incompressibility, the mass conservation requires

$$\nabla \cdot \mathbf{v} = 0. \tag{2}$$

Besides the governing equations, the model involves two boundary conditions; a non-slip boundary ($\mathbf{v} = 0$) at a glass-silicon interface and a surface tension driven free glass-gas interfaces that satisfy

$$\mathbf{n} \cdot \mathbf{T} = (-P_{ext} + \Gamma\gamma)\mathbf{n}, \tag{3}$$

where $\mathbf{n}$ is the outward unit normal, $\mathbf{T}$ is the total stress tensor acting on the fluid, P_{ext} is the external pressure, Γ is curvature of the interface, and γ is the surface tension.

III. METHOD

A. Fabrication process

(100)-oriented n-type silicon wafers (525 μm thick, 100 mm diameter) were used. The process started with a single-step standard photolithography (SUSS Microtec MA6) to pattern trench structures (10 mm long) with a width varying from 1.5 μm to 4 μm. Next, anisotropic etching of silicon was accomplished in a deep reactive ion etching (DRIE) chamber (STS ICP Silicon Etcher). The Si etching involved multiple cycles of etch and passivation steps depending on the depth required ranging from 2.5 to 8 μm. Each cycle began with an etch step (45 sccm SF_6, 5 sccm O_2, 15 sccm C_4F_8, 600/8 W coil/platen power for 7 s), followed by a passivation step (75 sccm C_4F_8, 200 W coil power for 5 s). Subsequently, a layer of phosphosilicate glass (PSG) 5 μm thick was deposited on the structured silicon wafers through a low-pressure chemical vapor deposition (LPCVD) process (420 °C, 180 mTorr) in a furnace (ASM LB 45 LPCVD). The phosphorus (P) content of PSG varied in 7.5–10 mol. %, as confirmed by X-ray

fluorescence (JEOL JSX-3201Z element analyzer). Finally, thermal anneal of the wafers was conducted either in a diffusion furnace (ASM LB45) or in a rapid thermal processor (RTP-300) for the stated durations and temperature levels. Fabricated structures were cleaved perpendicular to the trenches to expose their cross-sectional profiles for scanning electron microscopy (SEM) inspection and for fluidic access.

B. DNA stretching experiments

For the DNA stretching experiments, EcoR I digested λ-phage DNA (Sigma) was prepared in $0.5\times$ TBE buffer (0.045 M tris-base, 1 mM EDTA with 0.045 M boric acid) at a concentration 1 μg/ml. The DNA was labeled with intercalating dye SYBR Green (Sigma) with 1 dye molecule per 2.5 bp and loaded into the nanocapillaries under capillary action. Labeled DNA was imaged by a CCD camera on a microscope with a $40\times$ water immersion objective and a laser-induced fluorescence setup as previously described.[34]

C. Simulations

The numerical simulation was conducted under COMSOL MULTIPHYSICS Software. Time-dependent 2-D Stokes equations were coupled with moving mesh method to track the gas-liquid interface and the boundary conditions were set as prescribed above. The viscosity of PSG (7.5 mol. % P) was calculated as 5.8×10^{11} Pa s using Arrhenius equation: $\mu(T) = \mu_0\exp(E/RT)$, where T is temperature (1000 °C), μ_0 is pre-exponential coefficient (3.8×10^{-14} Pa s), E is activation energy (6.14×10^5 J/mol), and R stands for the universal gas constant (8.314 J/mol K). The surface tension and the density of glass were assumed 300 N/m and 2200 kg/m^3, respectively.[36] Both the internal pressure of glass and the pressure inside the voids were set equal to the glass deposition pressure (180 mTorr). The ambient pressure was assigned as 1 atm.

IV. RESULTS AND DISCUSSIONS

A. Baseline process

Figs. 2(a) and 2(b) show SEM images of a 5 μm thick PSG layer (7.5 mol. % P) deposited on a silicon wafer pre-structured with an array of 2 μm wide and 2.5 μm deep trenches apart by 5 μm in nominal values. Due to the non-conformal deposition profile, trenches were enclosed

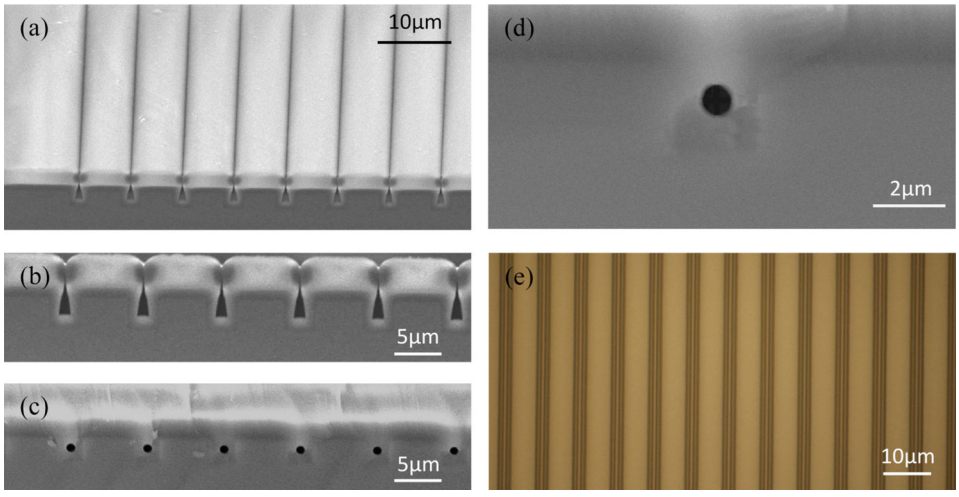

FIG. 2. SEM images: (a) oblique and (b) cross-sectional view of voids being trapped within rectangular silicon trenches due to non-conformal deposition of glass; (c) cross-section of the same voids after being transformed into cylindrical capillaries Ø800 nm via 2-h anneal at 1000 °C; (d) a close-up shot on a single capillary. (e) A micrograph of the Ø800 nm capillaries from above seen as continuous bright stripes aligned within dark stripes (silicon trenches).

by the glass filling, which left voids of a triangular cross-section profile trapped inside. The non-conformal deposition profile can be mainly attributed to a geometric shadowing effect in LPCVD chamber whereby the reactant species reaching the substrate surface follow straight-line trajectories and those already deposited on the top corners of a trench begin to obstruct the line of sight from the bottom corners to the reaction chamber.[37] This phenomenon, given the slow surface migration of the reactant species adsorbed on the low-temperature substrate, causes the non-uniform film thickness observed across the trench, much thicker near the top surface but thinner inside the trench. Eventually, the thicker top region pinches off, enclosing the trench before it gets completely filled. Fig. 2(c) reveals SEM cross-section of the same structure after thermal anneal in a 1000 °C diffusion furnace for 2 h. It is clear that the voids underwent shape transformation driven by surface tension and turned them into nearly identical cylindrical capillaries. Fig. 2(d) closes onto a single capillary buried inside a silicon trench and verifies the diameter already reached $<1\,\mu$m (Ø800 nm). It is our claim that the diameter can be further shrunk below 100 nm with an extended anneal. Fig. 2(e) depicts a representative optical micrograph of the capillaries (Ø800 nm), where they appear from above as highly regular thin bright stripes aligned within dark stripes (silicon trenches). Each pair of the dark stripes refers to the PSG layers deposited on the opposing sidewalls of a trench, sandwiching a thin bright stripe, the cylindrical capillary, enclosed therein. One can deduce from the image that the trenches ended up slightly wider ($2.2\,\mu$m) than the mask design. It is clear that the near-identical consistency of the capillary cross-sections continues throughout their length.

To validate our claim, the glass reflow process was simulated for a single trench using the dimensions specified for the above structure. Fig. 3 displays the simulation results describing the velocity profile that leads the shape transformation shown at the intermediate steps of thermal anneal. The simulation was commenced with a profile asymptotic to as-deposited glass ($t=0$) in Fig. 2(b). As can be seen, the reflow speed is considerably higher adjacent to the sharply curved free interfaces near the outer surface, while it remains relatively low near the trench bottom despite the comparably sharp curvatures and thus high Laplace pressure therein. The proximity of these sharply curved interfaces to the no-slip trench walls retards the fluid flow and, along with the viscous dissipation,[38] restricts the supply of extra material to the trench bottom. After an hour anneal, the top surface of the glass becomes nearly flat and the upper sharp curvature of the void gets rounded. With a half-an-hour additional anneal, a fully round void is attained at a diameter $\sim 1\,\mu$m, whereas the diameter further shrinks to $\sim$800 nm at the conclusion of a 2-h anneal, concurring with the fabricated profile [Fig. 2(d)]. As can be noticed, further anneal beyond this point ($t \geq 2.5$ h) continues to shrink the size below 400 nm but at a slower pace since the flow speed around the void gets lower. Although the flow appears to compress and distort the round shape, the shape distortion is not encountered in our fabrication process as presented later. Once a round shape is reached, it is preserved throughout the

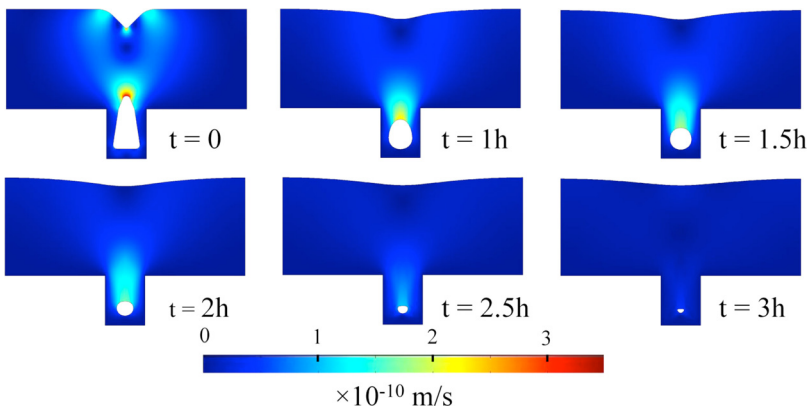

FIG. 3. Simulation plots mapping the velocity profile and the shape transformation across a glass layer deposited 5 μm thick over a trench 2 μm wide and 2.5 μm deep shown at different time intervals of 1000 °C reflow.

annealing process. The discrepancy with the simulation in this sub-micron regime may arise from the shape distortion of the over-stretched mesh elements near the void-glass interface or other plausible effects ignored in the model (e.g., non-uniform viscosity). Nevertheless, the qualitative description of the rounding effect is well captured in the simulation, which also hints at a shrinking trend of the round capillary with the further anneal.

B. Influence of the aspect ratio of trenches

Next, the impact of the trench aspect ratio (AR) on the glass thermal reflow process is investigated. The intuition suggests that the trench aspect ratio might influence the glass thermal reflow through two conflicting mechanisms. First, it may dictate the shape profile of the as-deposited glass layer that eventually determines surface forces driving the reflow. Second, it may impose a fluidic resistance that sets dissipative forces countering the reflow. Thus, there may exist an optimum AR for which the shape transformation occurs favorably within a practical anneal time.[31,32] Figs. 4(a) and 4(b) show SEM cross-sections of the evolved voids buried in silicon trenches encompassing six distinct combinations of nominal widths, 1.5, 2.0, and 2.5 μm, and depths, 2.5 and 8 μm, thereby, addressing low AR (1.7, 1.3, 1.0) and high (5.3, 4, 3.2) AR trenches, respectively. The results indicate that, in low AR trenches, reflow for 2 h is sufficient to return nearly identical round voids, on the same substrate, with a sub-micron diameter (900, 800, and 350 nm, respectively) whereas, in high AR trenches, doubling the anneal time has yet to form round capillaries mainly due to retarded reflow in such deep structures. It should be noted that the wider the trench gets, the more the capillary shrinks, a characteristic, which favors coarse patterning. Fig. 4(c) shows the simulated evolution of the void shape over time in a trench 2 μm wide and 8 μm deep (AR = 4) and can be directly compared to the shape evolution in a trench with the same width but the depth 2.5 μm (AR = 1.3) as shown in Fig. 3. Note that the identical velocity scales apply. Given the same trench width, no significant difference can be found between the as-deposited shape profiles, apart from the void elongation into the trench, particularly around the points of high curvature. Thus, the forces acting on the free

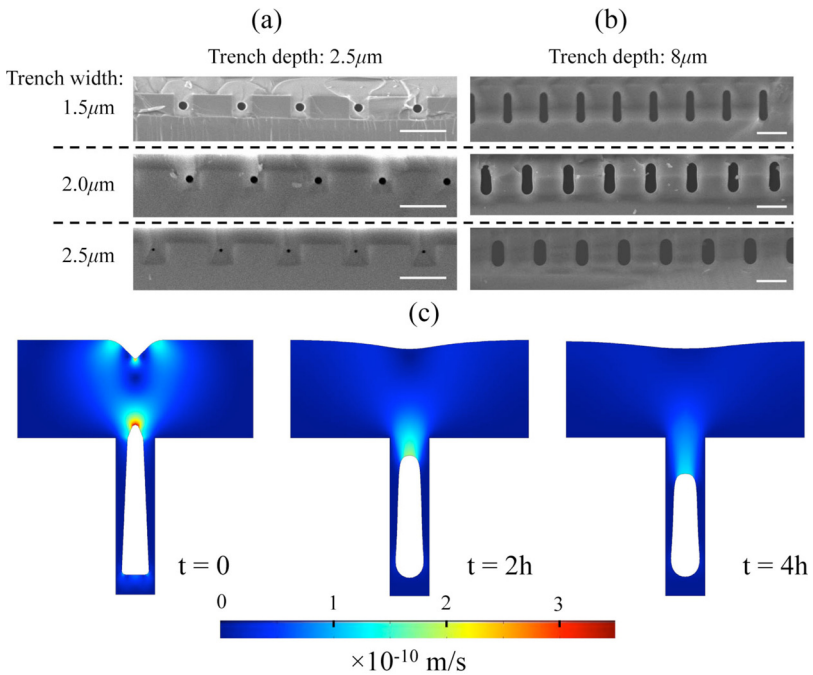

FIG. 4. SEM cross-sections of trenches having a nominal width of 1.5 μm, 2.0 μm, and 2.5 μm and depths (a) 2.5 μm and (b) 8 μm deposited with a 5 μm glass layer and underwent reflow at 1000 °C for (a) 2 h and (b) 4 h; scale bars: 5 μm. (c) Simulation plots mapping the velocity profile during 1000 °C reflow over different time intervals, showing the shape transformation of a void in a glass layer deposited 5 μm thick over a trench 2 μm wide and 8 μm deep.

interfaces and the flow speed should be comparable at the onset of the reflow. It is trivial that the void elongated into the deeper trench (high AR) must take longer time to evolve, as it has more space to fill. However, when the progress is evaluated at the end of a 2-h anneal, one can appreciate that such relation is unlikely to be linear as less volume gets filled in the high AR trench due to larger viscous dissipation along the void. These results support square-like trenches with a low AR ($\sim$1) as a more favorable surface topography for the formation of nanocapillaries.

C. Influence of the substrate surface topography

It should be noted that a complete enclosure of a silicon trench prior to thermal reflow of glass is an important prerequisite for the formation of a cylindrical buried capillary. Otherwise, the surface curvature of an unsealed configuration might drive the shape evolution to the opposite direction such that it leads to an open groove rather than a buried capillary. Depositing a sufficiently thick glass layer ensures the full enclosure. However, our fabrication results suggest that the choice of the underlying surface topography may favor the formation of buried capillaries even if their precursor voids were not completely sealed. Figs. 5(a) and 5(b) depict SEM cross-sections of 4 μm wide and 5.5 μm deep trenches deposited with 5 μm PSG (7.5 mol. % P) underwent 2-h and/or 4-h reflow at 1000 °C. Both structures differ in their spacing between the adjacent trenches, 10 μm and 5 μm, respectively. A closer inspection of the structures prior to reflow reveals that the voids are not completely closed as there are sub-micron gaps left above the voids where the expected glass pinch off should have taken place. An interesting observation is noted in the latter design (5 μm spacing) at the conclusion of a 4-h reflow, which cannot be seen in the former (10 μm spacing); every other trench gets a buried capillary while the remaining trenches are found further opened up. A quick check on the design at an intermediate step (2-h reflow) shows all the trenches ready to close with the glass layer barely pinching off in all. To better understand the mechanism behind this pattern formation, we simulated both structures and found indeed that the trenches apart by 10 μm are unable to form buried capillaries during reflow, while those apart by 5 μm are ready to pinch off at the end of a 2-h anneal. An excellent agreement can be seen between the fabrication profiles and their respective simulation results presented in Figs. 5(c) and 5(d). Noticing that the trenches apart by 5 μm are unlikely to pinch off at the same moment due to structural and process non-uniformities or simply randomness inherent in the process, we performed the rest of the simulation (beyond 2 h) having one of the trenches (arrow) set to pinch off first and managed to reproduce the pattern of the fabricated structure at the end of an extra 2-h reflow. We believe that as soon as a pinch off occurs in a trench, the high-energy surface subsequently created draws flow from the adjacent trenches to minimize the surface energy, thereby hindering the pinch-off about to happen in them. Thus, the trench sandwiched between the two sealed capillaries further opens up. Although one could take advantage of the surface topography to enclose capillaries dynamically

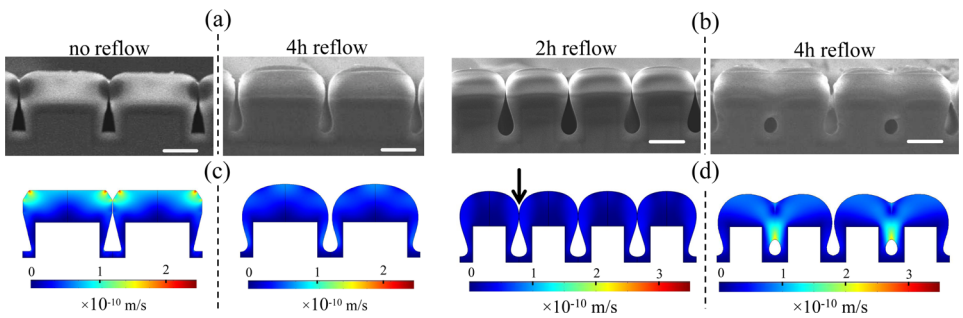

FIG. 5. SEM cross-sections of 4 μm wide, 5.5 μm deep trenches deposited with a 5 μm glass layer shown either as-deposited (no reflow) or underwent reflow at 1000 °C for the stated anneal time. The spacing between the adjacent trenches: (a) 10 μm and (b) 5 μm. Scale bars: 5 μm. Simulation plots (c) and (d) correspond to the fabricated profiles in (a) and (b), respectively, and indicate simulated shape profile and flow velocity distribution within the glass layer.

during reflow, this would be hard to control and better to avoid by ensuring the enclosure before the reflow.

D. Influence of the anneal temperature and duration

Once the surface topography in relation to the thickness and composition of the glass layer is fixed, including the aspect ratio and density of trenches, one has left with the anneal temperature and time to control shrinking of the capillaries below 100 nm. Performing anneal at a higher temperature further reduces the viscosity and increases the flow speed, which may pose a tighter window of control. For a fixed temperature, an extended anneal may cause the voids completely filled. The controllable shrinking of large voids into nanocapillaries was investigated on trenches with a width 1.5, 2.0, 2.5, and 3.0 μm, and a depth 2.5 μm, corresponding to a low AR (1.7, 1.3, 1.0, and 0.8) in which the rounding effect can occur in a reasonable time as verified by the results in Fig. 4. On these trenches, a glass layer was deposited 5 μm thick and with a relatively high phosphorous content (10 mol. % P) to ease the flow and shortened the overall anneal to minutes so that the reflow can be conducted in a RTP for a more accurate control of the time. Fig. 6(a) illustrates the measured diameters of the fabricated nanocapillaries in a plot of RTP anneal time. Prior to RTP, the voids were pre-rounded in a diffusion furnace via 15-min anneal at 1000 °C. RTP was subsequently performed at 950 °C for better size control. As shown, for the stated trench depth and anneal conditions, the capillaries shrink more readily within trenches wider than 2 μm which can be conveniently registered through standard photolithography. Within trenches 2.5 μm wide, the diameter of capillaries falls from 400 to 100 nm in 140 s, before they get completely filled with an extra 70 s anneal, whereas within 3 μm trenches, 30 s anneal is enough to bring them down from 200 nm to 50 nm. Figs. 6(b) and 6(c) show representative cross-sectional images of the Ø50 nm capillary and this diameter was found consistent along the length with a relative standard deviation below 10% ($n > 20$).

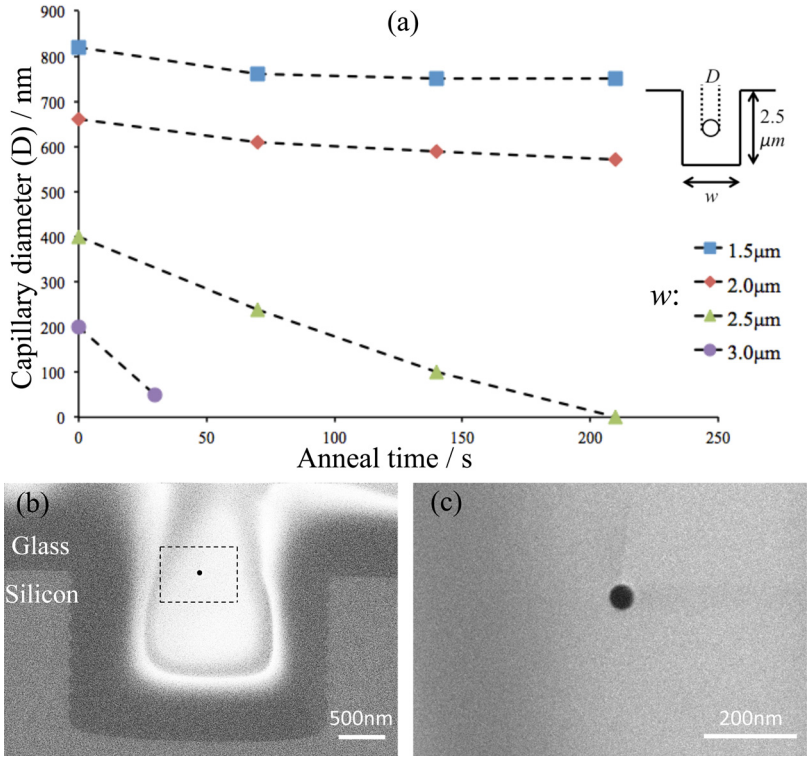

FIG. 6. (a) A plot of the measured capillary diameter as a function of RTP anneal (950 °C) time for increased trench widths (legend). Inset: a schematic description of the dimensions. (b) SEM cross-sectional image showing the Ø50 nm glass nanocapillary (inside the dashed rectangle) obtained in a trench 3 μm wide and 2.5 μm deep after 30 s anneal. (c) A close-up shot on the same nanocapillary.

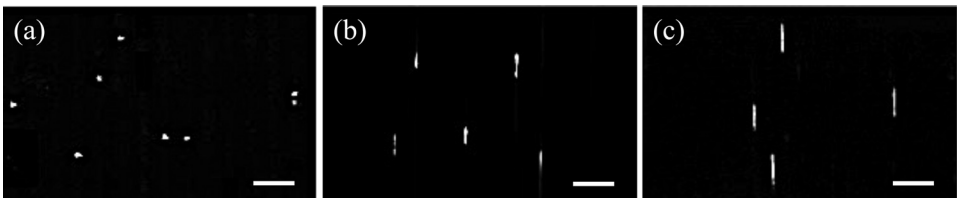

FIG. 7. Representative fluorescent micrographs showing λ-phage DNA strands in cylindrical glass nanocapillaries with a diameter (a) Ø400 nm, (b) Ø200 nm, and (c) Ø50 nm, fabricated in silicon trenches with a depth of 2.5 μm and a width of 2.5 μm in (a) and 3 μm in (b) and (c). Scale bars: 20 μm.

E. Stretching DNA in cylindrical glass nanocapillaries

The utility of the fabricated nanocapillaries was put to the test on the stretching of λ-phage DNA (48.5 kbp). It is well known that DNA in free solution coils itself randomly with a small radius of gyration (<1 μm for λ-phage DNA), whereas it gets stretched when physically confined in a channel of width or depth much smaller than the radius of gyration and about the same order as its persistence length (typically 50 nm for dsDNA). Reisner *et al.* used channels 30×40 nm and showed stretching of λ-phage DNA (in $0.5 \times$ TBE) to length 13 μm.[8] Xia *et al.* using 20×60 nm channels reported stretching of λ-phage DNA (in $0.5 \times$ TBE) to lengths between 11 and 13 μm.[28] Here, we examined stretching of λ-phage DNA also buffered in $0.5 \times$ TBE. Fig. 7 displays representative fluorescence micrographs of individual molecules captured inside the nanocapillaries of various diameters. It should be noted that, in a given array, not all the nanocapillaries could be found with molecules, at least in the field of view, since it is thermodynamically unfavorable for long DNA molecules to spontaneously uncoil in free solution and enter nanocapillaries directly under capillarity without the free energy needed to reduce entropy.[39] In the nanocapillaries having a relatively large diameter (Ø400 nm), the molecules preserve their recoiled shape appearing as fluorescent blobs [Fig. 7(a)]. Yet those confined in a smaller diameter (Ø200 nm) can be found stretched up to length 8.7 ± 1.2 μm ($n = 5$), about 47% of their dye-adjusted total contour length 18.5 μm [Fig. 7(b)]. Further confinement within even a smaller diameter comparable to the persistence length 50 nm, such as of those in Figs. 6(b) and 6(c), can lead to more effective stretching with the molecules reaching 14.1 ± 1.1 μm ($n = 10$), 76% of the contour length [Fig. 7(c)]. The molecules appear to be thicker than their actual size due to spreading of the fluorescent emission and the limited resolving power (diffraction limit) of the imaging system.[40] These results are consistent with the previous studies reported at the same ionic strength and indicate effective stretching of DNA in the integrated cylindrical glass nanocapillaries introduced here without relying on high-resolution lithography.

V. CONCLUSIONS

We have demonstrated a convenient and scalable method of fabricating cylindrical in-plane nanocapillaries. Unlike the previous demonstrations, our approach, which is based on reflow of an annealed glass layer for shape transformation of self-enclosed channels and their subsequent shrinking, avoids the advanced patterning techniques and rather prefers standard photolithography. Ironically, our simulation and fabrication results suggest that wider patterns (>2 μm) favor the formation of nanocapillaries as opposed to those narrower (~ 1 μm). Through numerical simulations, we have also shed light on the underlying mechanism and obtained shape profiles in excellent agreement with those fabricated. The nanocapillaries have been demonstrated as small as 50 nm in diameter and highly regular in profile over a large span (≥ 10 mm), thereby allowing effective stretching of digested λ-phage DNA as verified by fluorescence imaging microscopy owing to optically transparent nature of these nanocapillaries. The fabrication method shown here can be further extended to integrate the nanocapillaries with microchannels and fluidic inlet/outlet ports either by pre-structuring the substrate with a dual-step profile before depositing glass layer[34] or by simply dry etching the glass layer through a pattern.[33] We are

now investigating these routes of integration for novel nanofluidic devices towards biomedical applications.

ACKNOWLEDGMENTS

This project was financially supported by the Research Grant Council of Hong Kong, under the Early Career Scheme (Grant No. 623912).

[1]P. Abgrall and N. T. Nguyen, Anal. Chem. **80**, 2326 (2008).
[2]M. Napoli, J. C. T. Eijkel, and S. Pennathur, Lab Chip **10**, 957 (2010).
[3]J. O. Tegenfeldt, C. Prinz, H. Cao, S. Chou, W. W. Reisner, R. Riehn, Y. M. Wang, E. C. Cox, J. C. Sturm, P. Silberzan, and R. H. Austin, Proc. Natl. Acad. Sci. U.S.A. **101**, 10979 (2004).
[4]N. Douville, D. Huh, and S. Takayama, Anal. Bioanal. Chem. **391**, 2395 (2008).
[5]R. B. Schoch, J. Y. Han, and P. Renaud, Rev. Mod. Phys. **80**, 839 (2008).
[6]K. M. Zhou, J. M. Perry, and S. C. Jacobson, Annu. Rev. Anal. Chem. **4**, 321 (2011).
[7]W. Sparreboom, A. van den Berg, and J. C. T. Eijkel, Nat. Nanotechnol. **4**, 713 (2009).
[8]W. Reisner, K. J. Morton, R. Riehn, Y. M. Wang, Z. N. Yu, M. Rosen, J. C. Sturm, S. Y. Chou, E. Frey, and R. H. Austin, Phys. Rev. Lett. **94**, 196101 (2005).
[9]E. Abad, A. Juarros, A. Retolaza, S. Merino, R. Marie, and A. Kristensen, Microelectron. Eng. **88**, 300 (2011).
[10]Y. Kim, K. S. Kim, K. L. Kounovsky, R. Chang, G. Y. Jung, J. J. dePablo, K. Jo, and D. C. Schwartz, Lab Chip **11**, 1721 (2011).
[11]J. Han and H. G. Craighead, Science **288**, 1026 (2000).
[12]W. H. Guan, R. Fan, and M. A. Reed, Nat. Commun. **2**, 506 (2011).
[13]E. O. Gabrielsson, K. Tybrandt, and M. Berggren, Lab Chip **12**, 2507 (2012).
[14]M. Ali, S. Mafe, P. Ramirez, R. Neumann, and W. Ensinger, Langmuir **25**, 11993 (2009).
[15]L. J. Cheng and L. J. Guo, Chem. Soc. Rev. **39**, 923 (2010).
[16]I. Vlassiouk, S. Smirnov, and Z. Siwy, ACS Nano **2**, 1589 (2008).
[17]R. Karnik, C. H. Duan, K. Castelino, H. Daiguji, and A. Majumdar, Nano Lett. **7**, 547 (2007).
[18]R. Karnik, R. Fan, M. Yue, D. Y. Li, P. D. Yang, and A. Majumdar, Nano Lett. **5**, 943 (2005).
[19]S. W. Nam, M. J. Rooks, K. B. Kim, and S. M. Rossnagel, Nano Lett. **9**, 2044 (2009).
[20]I. Vlassiouk, T. R. Kozel, and Z. S. Siwy, J. Am. Chem. Soc. **131**, 8211 (2009).
[21]P. Chen, J. J. Gu, E. Brandin, Y. R. Kim, Q. Wang, and D. Branton, Nano Lett. **4**, 2293 (2004).
[22]R. B. Schoch, A. Bertsch, and P. Renaud, Nano Lett. **6**, 543 (2006).
[23]C. K. Harnett, G. W. Coates, and H. G. Craighead, J. Vac. Sci. Technol. B **19**, 2842 (2001).
[24]D. M. Koller, N. Galler, H. Ditlbacher, A. Hohenau, A. Leitner, F. R. Aussenegg, and J. R. Kren, Microelectron. Eng. **86**, 1314 (2009).
[25]L. J. Guo, Adv. Mater. **19**, 495 (2007).
[26]C. R. Song and P. S. Wang, IEEE Trans. Nanotechnol. **9**, 138 (2010).
[27]M. Fouad, M. Yavuz, and B. Cui, J. Vac. Sci. Technol. B **28**, C6i11 (2010).
[28]Q. F. Xia, K. J. Morton, R. H. Austin, and S. Y. Chou, Nano Lett. **8**, 3830 (2008).
[29]S. W. Nam, M. H. Lee, S. H. Lee, D. J. Lee, S. M. Rossnagel, and K. B. Kim, Nano Lett. **10**, 3324 (2010).
[30]S. Zankovych, T. Hoffmann, J. Seekamp, J. U. Bruch, and C. M. S. Torres, Nanotechnology **12**, 91 (2001).
[31]C. C. Wong, A. Agarwal, N. Balasubramanian, and D. L. Kwong, Nanotechnology **18**, 135304 (2007).
[32]A. Agarwal, N. Ranganathan, W. L. Ong, K. C. Tang, and L. Yobas, Sens. Actuators, A **142**, 80 (2008).
[33]W. L. Ong, J. S. Kee, A. Ajay, N. Ranganathan, K. C. Tang, and L. Yobas, Appl. Phys. Lett. **89**, 093902 (2006).
[34]Z. Cao, K. Ren, H. Wu, and L. Yobas, Biomicrofluidics **6**, 036501 (2012).
[35]C. A. Morris, A. K. Friedman, and L. A. Baker, Analyst **135**, 2190 (2010).
[36]G. Thallikar, H. Liao, T. S. Cale, and F. R. Myers, J. Vac. Sci. Technol. B **13**, 1875 (1995).
[37]T. S. Cale and G. B. Raupp, J. Vac. Sci. Technol. B **8**, 649 (1990).
[38]J. Koo and C. Kleinstreuer, Int. J. Heat Mass Tranfer **47**, 3159 (2004).
[39]H. Cao, J. O. Tegenfeldt, R. H. Austin, and S. Y. Chou, Appl. Phys. Lett. **81**, 3058 (2002).
[40]M. M. Frigault, J. Lacoste, J. L. Swift, and C. M. Brown, J. Cell Sci. **122**, 753 (2009).